



Structural and catalytic differences in the effect of Co and Mo as promoters for Pt-based aqueous phase reforming catalysts

Paul J. Dietrich ^a, Fred G. Sollberger ^a, M. Cem Akatay ^b, Eric A. Stach ^d,
W. Nicholas Delgass ^a, Jeffrey T. Miller ^c, Fabio H. Ribeiro ^{a,*}

^a Purdue University, School of Chemical Engineering, W. Lafayette, IN 47907, United States

^b Purdue University, School of Materials Engineering and Birck Nanotechnology Center, W. Lafayette, IN 47907, United States

^c Argonne National Laboratory, Chemical Sciences and Engineering, Argonne, IL 60439, United States

^d Brookhaven National Laboratory, Center for Functional Nanomaterials, Upton, NY 11973, United States

ARTICLE INFO

Article history:

Received 7 September 2013

Received in revised form 24 February 2014

Accepted 4 March 2014

Available online 19 March 2014

Keywords:

Aqueous phase reforming

Pt bimetallic catalyst

Operando X-ray absorption spectroscopy

Hydrogen production from biomass

ABSTRACT

Reaction rates (site time yields, normalized to CO chemisorption sites) and product selectivity were determined for PtCo, PtMo, and Pt supported on multi-walled carbon nanotubes for aqueous phase reforming of glycerol. The bimetallic PtCo and PtMo catalysts had 4.6× and 5.4× higher glycerol consumption rates than Pt, and 3.9× and 0.6× rates in H₂ formation compared to Pt. Hydrogen generation selectivity was similar on Pt and PtCo, but PtMo had an increase in selectivity to C—O cleavage products, which reduced H₂ yield at conversions over 60% (85–90% hydrogen yield for Pt and PtCo, 65% for PtMo). X-ray absorption spectroscopy and scanning transmission electron microscopy results indicate that PtCo adopts multiple mono- and bimetallic structures (Pt shell/Co core, well-mixed alloy, Pt only), which maintain surface Pt sites that are selective to hydrogen generation while adding a promotional metal that increases reaction rates. This is in contrast to a previously characterized PtMo catalyst which introduced surface sites capable of deoxygenation reactions (in the form of Pt—Mo metallic or Pt—MoO₄/OH acid pairs) which result in the observed decrease in selectivity.

© 2014 Elsevier B.V. All rights reserved.

1. Introduction

As economies look to transition away from petroleum as a basis for the fuels and chemicals industries, biomass will continue to attract attention as a renewable feedstock. However, due to its high oxygen content, significant quantities of hydrogen must be added to effectively deoxygenate the feed molecules [1–3]. One route that has been shown as technically feasible for hydrogen generation from biomass is aqueous phase reforming (APR) of oxygenated hydrocarbons with Pt-based catalysts [4,5]. The advantage of these reactions is that they are thermodynamically favorable (K_{eq} on the order of 10⁸ at 500 K) [4,6] and operate at mild conditions (200–260 °C, 15–60 bar) [4,7,8], which allows for relatively low temperature processing that will not result in the decomposition of the non-volatile sugar feedstocks [5].

Previous work on APR has focused mainly on the effects of catalyst formulation (metals loading and support) and process conditions on APR rates and selectivity. Aqueous phase reforming has been studied over a variety of active metals, with Pt and Ni found to be the most effective [9]. However, Ni generally has lower H₂ selectivity than Pt [9–11]. Palladium has been shown to be highly selective, but has generally lower rates than Pt [9]. The addition of a second promoter metal to Pt and Pd has been shown to enhance the rates of reaction under aqueous phase conditions [10,12,13]. In addition, the promoter may also be chosen to tune product selectivity to generate monofunctional liquid phase intermediates, which can be utilized in further processing to make liquid fuels [14,15]. Carbon is generally the support of choice as it has high activity and stability under aqueous phase conditions when compared to metal oxide supports [16].

Changing reaction conditions can also have an effect on the product distributions. Aqueous phase conditions take advantage of the water–gas shift reaction to produce product streams with low CO content, suitable for H₂ generation for fuel cell applications [4,5,7,8].

In this work, the focus is on understanding the constituent reactions of oxygenated hydrocarbons within APR, particularly those

* Corresponding author at: Purdue University, School of Chemical Engineering, 480 Stadium Mall Drive, W. Lafayette, IN 47907-2100, United States.

Tel.: +1 765 494 7799.

E-mail address: fabio@purdue.edu (F.H. Ribeiro).

with characteristics similar to biomass-derived sugars, and how to selectively turn these compounds into hydrogen by focusing on the relationship between materials properties and catalytic activity. Previously, we have characterized a PtMo bimetallic reforming catalyst, and concluded that while it increased the rates of reforming reactions, it had an undesirable side effect of reducing selectivity due to the presence of surface Mo [17,18]. Here, we describe the effects of promoting a multi-walled carbon nanotube (MWCNT) supported Pt catalyst with Co for hydrogen generation via APR. Cobalt was chosen as a representative 3d metal promoter, which have been demonstrated in both theoretical and experimental studies as effective promoters for biomass reforming [10,19–21]. Multi-walled carbon nanotubes have been shown to be effective supports for aqueous phase reforming catalysts [21–23], in addition to being TEM friendly. Here, we combine X-ray absorption spectroscopy and electron microscopy characterization with reaction kinetics using glycerol as a model compound to show how adding Co to a Pt-based reforming catalyst affects particle morphology, reaction rates, and product selectivity. We also compare the results to those for a Mo promoted Pt catalyst. We demonstrate that adding Co as a promoter creates bimetallic particles with generally Pt rich surfaces and increases the rates of reaction and hydrogen production while maintaining hydrogen selectivity above 90% at conversion above 60%.

2. Experimental methods

2.1. Catalyst synthesis

Four catalysts were prepared for this study, monometallic Pt and Co and bimetallic PtCo and PtMo catalysts. The multi-walled carbon nanotubes (MWCNT) support (CheapTubes, Inc.) was oxygen-functionalized by refluxing in concentrated (69 wt%) nitric acid for 4 h. The MWCNTs were then washed 10 times by centrifugation and decanting and dried overnight at 150 °C. The metals were then added by sequential incipient wetness impregnation (IWI) of aqueous solutions of tetraammineplatinum(II) nitrate (Sigma-Aldrich), followed by either those of cobalt nitrate hydrate (Alfa Aesar) or ammonium heptamolybdate tetrahydrate (Aldrich), with an intermediate drying step. Each solution was prepared so as to give 5 wt% Pt and a loading of Co or Mo equivalent to a molar ratio of 1:1 for Pt:Co or Pt:Mo (1.6 wt% Co, 2.6 wt% Mo). The monometallic Co catalyst was prepared by IWI with an aqueous solution of cobalt nitrate hydrate (Alfa Aesar) leading to a metal loading of 5 wt%. The catalysts were dried in air overnight at 150 °C following impregnation. Before starting the reaction, each catalyst was reduced *in situ* with 45 sccm of a 5% H₂/Ar mixture using a 2 h ramp, 2 h soak to 400 °C for Pt/MWCNT and PtCo/MWCNT and 450 °C for PtMo/MWCNT and Co/MWCNT.

2.2. Reaction kinetics measurements

Aqueous phase reforming kinetic experiments were conducted in a fixed bed, plug flow reactor system, equipped to perform *operando* X-ray absorption spectroscopy [24]. Sigradur glassy carbon tubes (10 mm/4 mm OD/ID, Hochtemperatur-Werkstoffe GmbH) were used as reactors, as they have been shown to have good X-ray transparency under operation at temperatures and pressures up to 600 °C and 35 bar [25]. These reactors were connected using graphite ferrules and standard Swagelok fittings. Catalyst samples were held in place by plugs of quartz wool and mesh frits welded to the end of stainless steel rods. The catalyst loading was varied between 30 and 200 mg. Prior to introduction of the liquid feedstock, the catalysts were reduced *in situ* at the conditions described in Section 2.1. Reforming experiments

were conducted isothermally at 230 °C and 32 bar, with a 30 wt% aqueous glycerol solution pumped into the system using a Tele-dyne ISCO syringe pump (100DM). Flow rates were varied between 0.01 mL/min and 0.3 mL/min, corresponding to weight hourly space velocities (WHSV, gram glycerol/(gram catalyst × h)) between 1 h⁻¹ and 200 h⁻¹, to control glycerol conversion. Temperature was monitored and controlled via a type K thermocouple (Omega Engineering) inserted into the top of the catalyst bed and a PID controller (Omega Engineering). The system pressure was controlled via a back pressure regulator (GO Regulators). The reaction conditions and catalyst materials were chosen such that the system was under kinetic control (see the supplementary information for additional details).

Gas phase products were collected and analyzed online by continuously flowing 27 sccm of Ar as an internal standard through the liquid/gas phase separator. The Ar/product mix was then fed into two gas chromatographs (Agilent 6890 and 7890) equipped with packed columns (Carboxen-1000) and thermal conductivity detectors. Helium (for detecting gas phase CO_x and hydrocarbon species) and nitrogen (for detecting hydrogen) were used as carrier gases. Samples of the liquid phase effluent were collected periodically and analyzed off line using an Agilent 7890 with a capillary column (DB-WAX) and an autosampler (Agilent 7693). System mass balances generally closed to within 100 ± 2%, and system carbon balances generally closed to within 100 ± 5%. The system carbon balance accounts for all products in gas and liquid phase, as well as the unreacted feed.

Reaction rates are defined as site time yields (STY, mol product/(mol Pt × s)), and are normalized by surface sites from CO chemisorption (PtMo/MWCNT and PtCo/MWCNT catalysts) and H₂ chemisorption (Pt/MWCNT catalyst). Rates are defined as site time yields as the nature of the reaction (series/parallel reaction with many intermediates and several sequential reaction steps) makes differential operation difficult to achieve. Individual product rates are defined as r_x (where x is glycerol or a reaction product, i.e. r_{methane} is the methane rate). Errors on the measured STYs were based on a 95% confidence interval of 4 repeat points at the same conditions. Carbon selectivity is defined as (($r_{\text{product}} \times \text{Carbon number}/(r_{\text{glycerol}} \times 3)$) × 100%), and is calculated to sum to a total of 100% over all the products in both liquid and gas phase effluents. Hydrogen selectivity in the gas phase compares the amount of molecular H₂ generated versus hydrogen contained in alkanes, and is calculated as $r_{\text{H}_2}/(r_{\text{H}_2} + 4 \times r_{\text{CH}_4} + 7 \times r_{\text{C}_2\text{H}_6}) \times 100\%$.

The rates here are defined as site time yields, rather than turnover rates, due to the complexity of the glycerol reforming reaction network. Because of the many reaction intermediates and interconnected network of series and parallel reactions with possible inhibition by the products, achieving differential conditions would require a much more detailed kinetic study. It is possible to co-feed the liquid phase intermediates along with the glycerol, but as these molecules are formed from and react to form the same products as glycerol, deconvoluting the contribution to the measured rates from all the molecules in the feed would be difficult. These non-differential conditions are why the reaction rates are defined as a site time yield rather than a turnover rate. In this paper, the site time yields are compared at small glycerol conversion (1%), ensuring that feed molecule concentration is constant throughout the bed. However, we do not know the concentration profiles of the intermediates and products from the reaction, because each can either desorb from the surface or continue to react. Therefore, the local concentrations of the intermediates will be affected by the flow conditions within the reactor, or in our case the pump speed. To minimize the effects of flow patterns on the concentration profiles, and therefore their effect on the measured site time yields, all the STY presented here were measured at the same flow conditions, with the same WHSV and similar catalyst loadings and pump

speeds. For the experiments comparing the site time yields, the pump speed was 0.3 mL/min with 50 mg of catalyst, corresponding to a WHSV of 110 h⁻¹. Keeping these variables constant allows for us to compare the site time yields relative to one another, but may make comparison with other sources impractical, unless they are operating under the same flow conditions.

The turnover rates of water–gas shift (WGS) and methanation reactions were measured simultaneously in a fixed bed, plug flow reactor. Reaction rates for the water–gas shift reaction are defined as mol H₂ formed/(mol Pt × s), normalized to total Pt loading, and were measured at 300 °C. Reaction rates for the methanation reaction are defined as mol CH₄ formed/(mol Pt × s). The experiments were performed at conditions to ensure a differential reactor, i.e. less than 10% CO conversion and product co-feed. Feed concentrations were 6.8% CO, 8.5% CO₂, 21.9% H₂O, 37.4% H₂, and balance Ar flowed at 75 sccm at atmospheric pressure. For additional experimental details on the water–gas shift reaction, see [26].

2.3. X-ray absorption spectroscopy experiments

Platinum L_{III} (11.564 keV) and Co K (7.709 keV) edge X-ray absorption spectroscopy (XAS) experiments were performed at the Materials Research Collaborative Access Team (MRCAT) insertion device (10-ID) and bending magnet (10-BM) beamlines at the Advanced Photon Source (APS), Argonne National Laboratory. All experiments reported were conducted in transmission mode. Ion chambers were optimized for maximum current with linear response (ca. 10¹⁰ photons detected s⁻¹). A third detector in series simultaneously captured a reference foil for energy calibration for all XAS experiments. The X-ray beam size was 0.5 mm × 0.5 mm (*operando* experiments) and 1.5 mm × 0.5 mm for *ex situ* and *in situ* experiments.

Ex situ and *in situ* experiments were conducted in a quartz tube reactor (1 in. OD, 10 in. length) with Kapton windows sealed with Ultra-Torr fittings. Ball valves were connected to the tubes by welded Swagelok fittings to provide a gas inlet and outlet and to isolate the catalyst atmosphere. Catalyst samples were pressed into self-supporting wafers loaded into a 6 well sample holder. The amount of catalyst in each well was calculated to give an absorbance ($\mu\chi$) of approximately 2.0. Catalysts were reduced in 3.5% H₂/He mixture at the appropriate reduction temperature (see Section 2.2), then purged with He for 10 min and cooled to room temperature prior to scanning. Catalysts with adsorbed CO were first reduced, treated with a mixture of 1% CO/He at room temperature, purged with He for 10 min at room temperature, and scanned under a static He atmosphere.

Operando XAS experiments were performed under liquid phase reaction conditions identical to those described in Section 2.2. Multiple scans were taken and averaged at steady state conditions to obtain adequate signal to noise. The Debye–Waller factor (DWF, $\Delta\sigma^2$) is temperature dependent, and the value at reaction temperature was determined by obtaining the XAS spectrum first at the reaction temperature and again after cooling to room temperature and assuming the same coordination number at both temperatures. Gas phase reaction products were continuously monitored to determine when the system had achieved steady state. Liquid products were collected in a manner similar to sampling in the lab after several hours at steady state and analyzed off line later to ensure consistency with lab results.

X-ray absorption spectra were analyzed using standard practices with WINXAS 3.1 software. X-ray absorption near edge (XANES) spectra were obtained using standard methods and were energy calibrated by comparing the standard edge position to the edge position of a simultaneously obtained foil. The edge energy was determined from the position of the maximum of the first peak in the first derivative of the XANES region.

Phase shifts and backscattering amplitudes for the extended X-ray absorption fine structure (EXAFS) were determined for monometallic scatterers (i.e. Pt–Pt and Co–Co) from experimental data obtained from the foils (12 scatterers at 2.77 Å for Pt–Pt; 12 scatterers at 2.51 Å for Co–Co). Bimetallic scatterers (Pt–Co and Co–Pt) were calculated with FEFF6 code using two atom calculations. The values for S_0^2 (amplitude reduction factor) and $\Delta\sigma^2$ were first determined by fitting the foils with FEFF. The EXAFS parameters were calculated for the first shell using these references by performing a least squares fit in R-space of the k^2 -weighted Fourier transform.

2.4. Transmission electron microscopy

The catalyst powder (1–2 mg) was suspended in pure ethanol (1–3 mL) and dispersed with an ultrasonic bath for approximately 5 min. Several drops of this suspension were spread over a copper TEM grid (200 mesh) coated with a lacey carbon film. The images were captured on an FEI Titan microscope operating at 300 kV and equipped with a Gatan Imaging Filter (GIF). Digital images were captured on a CCD camera (2048 × 2048 pixel) and stored using the Gatan Digital Micrograph software package. Particle size distributions on both fresh and used samples were determined using the ImageJ software package.

Scanning transmission electron microscopy (STEM) and electron energy loss spectroscopy (EELS) analyses were carried out using the dedicated aberration-corrected STEM Hitachi HD-2700C at 200 kV equipped with a modified Gatan Enfina ER spectrometer hosted at the Center for Functional Nanomaterials, Brookhaven National Laboratory. The convergence angle and the ADF collection angles were 28 mrad and 64–341 mrad, respectively. The Enfina spectrometer entrance aperture was set to 3 mm resulting in an EELS collection angle of 26.7 mrad and an energy resolution of 0.35 eV as measured from the full width at half maximum (FWHM) of the zero-loss peak.

The EELS spectra for Co and Pt were collected at the L_{2,3} and M_{4,5} edges, respectively. EELS line scans for Co and Pt were performed separately, the order of which was varied randomly to assess the effect of the condensed electron beam on the nanoparticles. The EELS dwell time was varied between 0.1–0.3 s to avoid beam induced structural changes. Any structural change can be discerned by comparing the HAADF line-scan print of particles under two successive line-scans. The data showing particles undergoing such a change were discarded. The step size for line-scans was varied between 1 and 3 Å. The core-loss intensities were extracted by extrapolating the background using a power-law model and subtracting it from the acquired signal. Data processing was carried out using Gatan Digital Micrograph.

3. Results

3.1. Glycerol reforming experiments

Product distributions for the glycerol reforming reaction were studied over PtCo/MWCNT, Pt/MWCNT, and PtMo/MWCNT, the latter two being the MWCNT supported analogs of activated carbon supported catalysts that had been previously characterized [17,18]. Glycerol was chosen as a model compound due to its C:O stoichiometry of 1:1 (typical of many biomass-derived compounds) and simple product distribution compared to five or six carbon sugar molecules.

The addition of Mo and Co to a Pt-based catalyst caused an increase in the site time yield (normalized to surface sites measured by CO chemisorption) of glycerol by factors of 4.6 for PtCo and 5.6 for PtMo at a conversion of 1%, indicating a promotional effect of

Table 1

Reaction site time yields (normalized to CO chemisorption sites) for MWCNT supported Pt, PtMo, and PtCo, and rate ratios for PtMo/Pt and PtCo/Pt. Site time yields measured at 230 °C, 32 bar, with WHSV = 110 h⁻¹. Water–gas shift and methanation rates were measured at 300 °C with 75 sccm feed of 6.8% CO, 8.5% CO₂, 21.9% H₂O, 37.4% H₂, and balance Ar at atmospheric pressure.

Catalyst	Site time yields/10 ⁻² s ⁻¹			STY ratios	
	Pt	PtMo	PtCo	PtMo/Pt	PtCo/Pt
Glycerol consumption	1.2	6.5	5.4	5.6	4.6
H ₂	7.1 ± 0.5	5 ± 2	28 ± 2	0.6	3.9
CO ₂	1.6 ± 0.1	2.9 ± 0.3	7.0 ± 0.2	1.8	4.4
CH ₄	0.18 ± 0.03	0.3 ± 0.1	0.29 ± 0.03	1.4	1.6
Ethylene Glycol	0.22 ± 0.03	1.0 ± 0.2	1.5 ± 0.2	5.5	8.2
Hydroxyacetone + Propylene Glycol	0.45 ± 0.05	3.1 ± 0.8	1.4 ± 0.3	7.5	3.5
Turnover rate/10 ⁻² s ⁻¹					
Water–gas shift	0.7	4.6	7.8	11	6.6
Methanation during WGS	0	0	0.1	—	—

each of the secondary metals on the reaction (Table 1). However, the STY of H₂ generation was lower on PtMo than Pt (4.6×10^{-2} versus 7.1×10^{-2} s⁻¹) at 1% conversion, whereas PtCo had a four-fold increase in the H₂ STY over the monometallic Pt (28×10^{-2} versus 7.1×10^{-2} s⁻¹) at the same conversion. Despite an apparent suppression of the H₂ STY, the PtMo had an increase in the site time yields of H₂ generation pathway products CO₂ and ethylene glycol by factors of 1.8 and 5.5. This difference in promotional effect is the result of selectivity differences in both liquid and gas phase products between the two catalysts.

Gas phase products identified in the reaction effluent include H₂, CO, CO₂, and CH₄. Carbon monoxide was not a major reaction product. When it was detected, CO₂:CO ratios were in excess of 100:1. Carbon selectivity ($r_{\text{product}} \times \text{Carbon number} / (r_{\text{glycerol}} \times 3) \times 100\%$) to CO₂ and CH₄ over Pt, PtMo, and PtCo catalysts is presented in Fig. 1. For all catalysts tested, CO₂ was the most prominent gas phase species, with CO₂:CH₄ ratios greater than 8:1. As previously reported, a CO₂:CH₄ ratio in excess of 0.74:1 will result in a net generation of hydrogen [17], suggesting that H₂ formation reactions are the dominant pathway for these catalysts. In general, Pt and PtCo had a higher selectivity to CO₂ versus PtMo, and a lower selectivity to CH₄, particularly at conversions above 10%. The gas phase hydrogen selectivity – which considers the hydrogen produced as molecular H₂ versus the hydrogen that is contained in hydrocarbons as a result of hydrogen consuming side reactions – is presented in Fig. 2. At all conversions, Pt and PtCo maintain

hydrogen selectivity above 85%, with PtCo having about 5% higher H₂ selectivity at all measured conversions. PtMo starts with a lower H₂ selectivity (82% for PtMo versus 96% and 90% for Pt and PtCo at conversion of around 1%), and has around 20% lower selectivity for conversion above 60%.

Liquid phase products in the reaction effluent were ethylene glycol, propylene glycol, hydroxyacetone, ethanol, acetaldehyde, methanol, 1-propanol, 1,3-propanediol, propionaldehyde, 2-propanol, and acetone. Liquid phase products have been grouped into either carbon–carbon ([C–C]) scission products (methanol, ethylene glycol) or carbon–oxygen ([C–O]) scission products (propylene glycol, hydroxyacetone, ethanol, 1- and 2-propanol, acetone, acetaldehyde, propionaldehyde, 1,3-propanediol). In general, the carbon selectivity in the liquid phase was dominated by [C–O] versus [C–C] cleavage products for all catalysts tested, with [C–O] scission selectivity ranging between 25% and 75% (Fig. 3a), and [C–C] scission selectivity ranging between 3 and 20% (Fig. 3b). A direct comparison of the catalysts (Fig. 3) shows that Pt and PtCo had higher selectivity to [C–C] cleavage products and lower selectivity to [C–O] products in the liquid phase versus PtMo. The selectivity to liquid phase products was similar over Pt and PtCo and different for PtMo at similar glycerol conversion, suggesting that Pt and PtCo had similar overall reaction pathways (see Section 4).

In addition to measuring the liquid phase reforming site time yields and selectivity of these catalysts, the rates of the gas phase

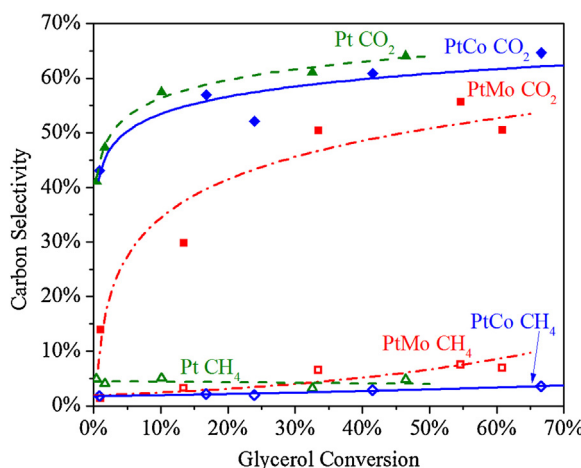


Fig. 1. Gas phase carbon selectivity to CO₂ (filled markers) and CH₄ (open markers) as a function of glycerol conversion for Pt (green, ▲), PtMo (red, ■), and PtCo (blue, ◆) catalysts at 230 °C, 32 bar, and WHSV between 1 and 200 h⁻¹. (For interpretation of the references to color in this figure legend, the reader is referred to the web version of this article.)

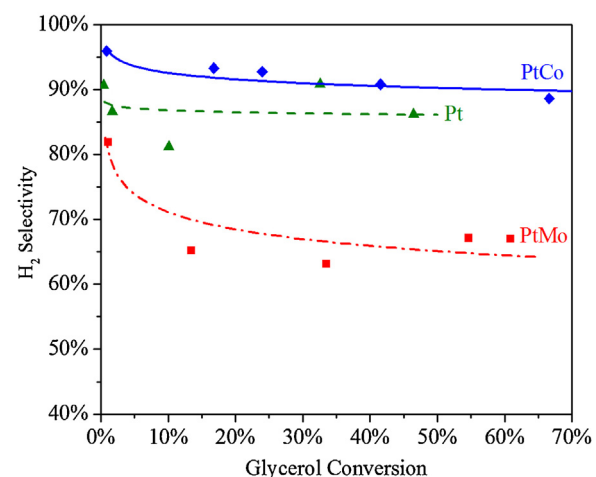


Fig. 2. Gas phase hydrogen selectivity as a function of glycerol conversion for Pt (green, ▲, dashed line), PtMo (red, ■, dashed/dotted line), and PtCo (blue, ◆, solid line) catalysts at 230 °C, 32 bar, 30 wt% aqueous glycerol feed, and WHSV between 1 and 200 h⁻¹. (For interpretation of the references to color in this figure legend, the reader is referred to the web version of this article.)

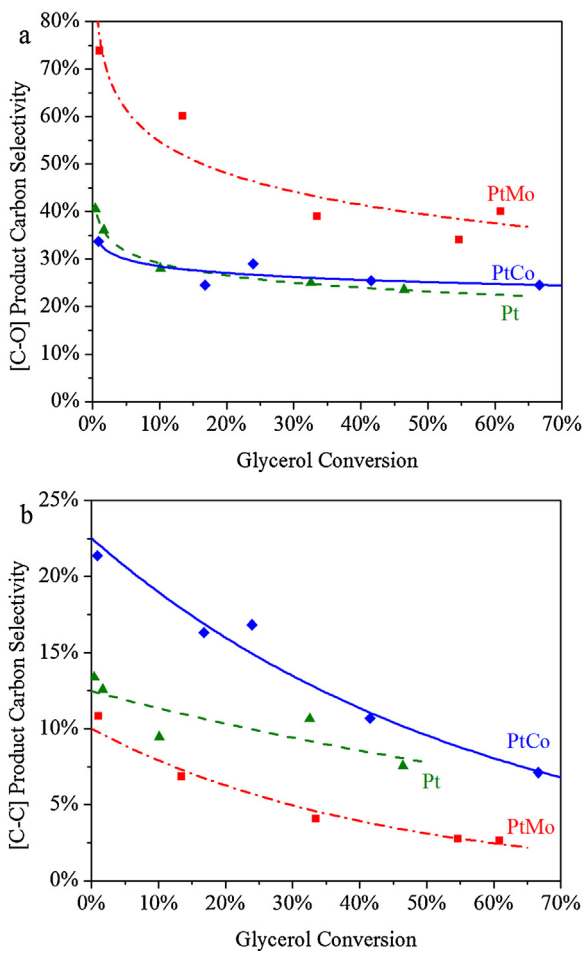


Fig. 3. Carbon selectivity to (a) [C—O] scission (combined carbon selectivity to propylene glycol, hydroxyacetone, ethanol, 1- and 2-propanol, acetone, acetaldehyde, propionaldehyde, and 1,3-propanediol) and (b) [C—C] scission (combined carbon selectivity to ethylene glycol and methanol) products as a function of glycerol conversion for Pt (green, ▲, dashed line), PtMo (red, ■, dashed/dotted line), and PtCo (blue, ♦, solid line). Values measured at 230 °C, 32 bar, and 30 wt% aqueous glycerol with WHSV between 1 and 200 h⁻¹. (For interpretation of the references to color in this figure legend, the reader is referred to the web version of this article.)

water–gas shift (WGS) and methanation reactions were also measured (Table 1). Both PtCo and PtMo had a promotional effect over the monometallic Pt catalyst, with a factor of 11 for PtCo and 6.6 for PtMo. Methanation activity was not observed on Pt or PtMo during WGS, but PtCo had a rate to methanation that was ~60 times lower than the WGS rate.

3.2. Catalyst characterization

3.2.1. Electron microscopy

Transmission electron microscopy (TEM) was used to determine the size and abundance of the metal nanoparticles before and after reaction. Representative TEM images for the PtCo/MWCNT and Pt/MWCNT catalysts are presented in Fig. S.1, for both fresh and used samples. After H₂ reduction and before APR, the PtCo catalyst had a particle size distribution of 1.0 ± 0.3 nm (Fig. S.2). After reaction for more than one week, the particle size increased to 2.1 ± 0.6 nm, and showed a broadening of the distribution (Fig. S.2). The fresh Pt/MWCNT catalyst had a particle size distribution of 1.1 ± 0.5 nm after reduction (Fig. S.2a), similar in size to the PtCo. After 8 days on stream, this catalyst had a particle size distribution of 2.1 ± 0.9 nm (Fig. S.2b). These results are in contrast to the results of our previous characterization on activated carbon supported

catalysts, which had fresh particle sizes of around 2 nm that sintered to 5 nm after reaction. These results suggest that the MWCNT support helps to disperse and stabilize the metal nanoparticles, as the size distributions on the used samples were similar to those for the fresh samples on activated carbon.

Scanning transmission electron microscopy (STEM) imaging was coupled with Electron Energy Loss Spectroscopy (EELS) to probe the configurations of nanoparticles present on used PtCo/MWCNT catalysts. Three different particle configurations were found based on how Pt and Co atoms coordinate themselves with respect to each other: Pt only, a Co core encapsulated by a Pt shell, and a well-mixed PtCo alloy. Fig. 4 shows representative HAADF-STEM and STEM-EELS line scans of the different particle configurations that have been assigned to this catalyst; a discussion of the assignment of these particle types based on the STEM-EELS line scans may be found in the Supplementary Information. We note that these images are not necessarily representative of particle size, that is, the Pt only particles are not necessarily smaller than the bimetallic particles. The particle in Fig. 4a consists of Pt shell covering a Co core, confirmed by a STEM-EELS elemental line scan (Fig. 4b). The particle at the far left in Fig. 4c is a Pt only particle, and the other particles in the same figure are well mixed PtCo alloys. Similar line scans were performed on 37 different nanoparticles on the catalyst sample, and the number and percentage of each type of configuration was tabulated (Table 2). The results suggest that there were a significant number of Pt only particles (59%), and fewer bimetallic particles having Pt shell/Co core (30%), and mixed alloy (11%). No Co only particles were observed.

The crystal structures of the core–shell particle depicted in Fig. 4a and the mixed alloy particle depicted in Fig. 4c were determined by taking the fast Fourier transformation (FFT) of high resolution STEM images (Fig. S.3b and d). The FFT patterns match those of face-centered cubic (FCC) zone axis patterns 0 0 1 and 1 1 0 for the core–shell and mixed alloy particles, respectively. The different facets of the nanoparticles are shown in Fig. S.3a and c. The available surface facets correspond to the lowest energy planes. Elemental Pt and Co have an FCC structure, which is observed in the bimetallic core–shell and mixed alloy particles.

3.2.2. X-ray absorption spectroscopy

X-ray absorption spectroscopy characterization was performed on the PtCo catalysts under *ex situ*, *in situ*, and *operando* conditions to determine the structural characteristics of the catalyst. The XANES results for the fresh catalyst at the Pt L_{III} edge compared to a Pt foil and the monometallic Pt/MWCNT catalyst are presented in Fig. 5a. Compared to the Pt foil, both Pt and PtCo catalysts show a decrease in the white line intensity, a characteristic of nanoparticles [27,28], indicating that the Pt is fully reduced. However, the PtCo edge position (Table S.1) is slightly shifted (by 0.3 eV) with a broader white line compared to the monometallic Pt catalyst, which is caused by the alloying of the two metals [17].

Analysis of the Co K edge XANES of the fresh catalyst (Fig. 5b) indicates that the Co is not fully metallic after reduction under H₂ at 400 °C. The white line intensity is between that of the CoO standard and the Co foil, indicating that the average Co oxidation state is between Co⁰ and Co²⁺. Fitting the XANES with a linear combination of Co²⁺ and Co⁰ references shows that the Co is 80% reduced after pretreatment. To probe the effects of the Pt on the Co oxidation state, a 5 wt% Co/MWCNT catalyst was subjected to the same pretreatment conditions as the bimetallic catalyst. This pretreatment reduced the Co, but to a lesser degree than the PtCo catalyst: 50% Co⁰ on the CoO_x/MWCNT catalyst versus 80% Co⁰ on the PtCo bimetallic.

The Fourier transform (FT) of the Pt L_{III} EXAFS of the fresh PtCo (Fig. 6) shows characteristics of bimetallic particles present on the catalyst. The changes in the magnitude and shifts in the zero of the

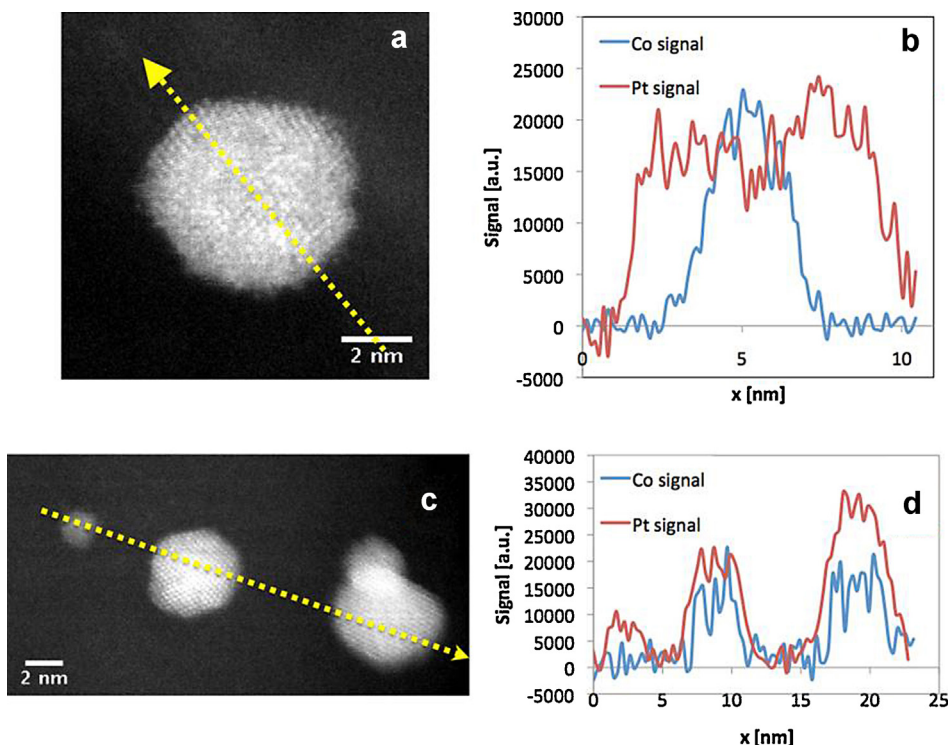


Fig. 4. (a) HAADF-STEM image and (b) STEM-EELS elemental linescan of a representative Pt shell/Co core particle. (c) HAADF-STEM image and (d) STEM-EELS elemental linescan of representative Pt only ($x=0\text{--}5\text{ nm}$), and mixed Pt/Co alloy particles ($x=5\text{--}10\text{ nm}$, $15\text{--}25\text{ nm}$). All images taken on a used PtCo/MWCNT sample.

imaginary spectra suggest the presence of a second backscattering atom in addition to Pt, i.e. Co. The fit parameters (Table S.1) include both Pt–Pt and Pt–Co coordination. The Pt–Pt bond distance is compressed relative to that for bulk Pt to 2.73 Å, similar to changes that are observed in monometallic Pt nanoparticles (2.72 Å). The low Pt–Pt coordination number (4.6) suggests a well-dispersed Pt phase. The Pt–Co coordination number (2.5) is similarly low, and the bond distance (2.60 Å) is about half way between a Pt–Pt and Co–Co bond (2.77 Å and 2.51 Å), which is indicative of the bimetallic nature of the particles.

The FTs of the Co K edge EXAFS of the fresh PtCo sample (Fig. 7) have small shifts in the peak position in the magnitude and imaginary part of the FT, which suggests the presence of a second backscattering atom, i.e. Co–Pt, consistent with the Pt edge. The fit parameters (Table S.1) show similar Co–Co (3.8) and Co–Pt (2.6) coordination numbers with bond distances of 2.51 and 2.61 Å. The Co–Pt coordination number matches with that determined for Pt–Co, which satisfies the relationship $\text{CN}_{a-b}\cdot(\text{atoms } a)=\text{CN}_{b-a}\cdot(\text{atoms } b)$ [29], which specifies that the bimetallic CNs be equal for catalysts with metal molar ratios of 1:1. Even though there was a measurable amount (20%) of Co^{2+} observed in the XANES, the presence of Co–O backscattering was not detected in the EXAFS due to its low concentration and weak scattering compared to the Co–metal peaks. The low total coordination numbers for Pt and Co edges (CN around 7) agree with the formation of nanoparticles of 1–2 nm observed in the TEM analysis [30].

The presence of significant Pt in the surface layer on the PtCo bimetallic structure is shown by changes in the XANES spectrum

with CO adsorption [31]. The Pt L_{III} edge is a 2p to 5d electron transition, and it has been previously demonstrated that the shape of the XANES is affected by changes to the 5d electronic structure, such as those caused by chemisorption of molecules such as CO [31,32]. The XANES is Pt-specific, so this technique shows only the contribution of CO adsorbed on Pt surface sites and is independent of any Co–CO interactions. Fig. S.4a shows the effects of adsorbing CO on a monometallic Pt catalyst. The edge shifts to higher energy and there is an increase in the white line intensity, consistent with the loss of electron density from the d-band due to Pt bonding with CO [33]. Fig. S.4b shows the results of the same experiment conducted on a fresh PtCo bimetallic catalyst, yielding a qualitatively similar change in the XANES. By performing a Δ XANES analysis [31] and subtracting the spectrum obtained in He at RT from the spectrum with adsorbed CO, the contribution to the changes in the XANES from the surface adsorbate can be isolated (Fig. 8). The Pt/MWCNT and PtCo/MWCNT have similar particle sizes as determined by TEM, meaning that the surface metal fraction is similar for both the Pt and PtCo catalysts. Using a linear combination fit with CO adsorbed on Pt as a reference, it was determined that the Δ XANES spectrum for PtCo was about 65% of that for Pt, meaning that 65% of the surface atoms on the particles of the PtCo catalyst were Pt.

3.2.3. Operando XAS

The *operando* XAS results for the PtCo under aqueous phase conditions show a particle configuration that is similar to that for the *ex situ* results. The *operando* Pt XANES (Fig. 9a) has a qualitatively

Table 2

Number and percentage of different PtCo bimetallic particle configurations as identified by STEM-EELS line scans.

	Total	Co only	Pt only	Mixed alloy	Pt shell/Co core
Number	37	0	22	4	11
Percentage	100%	0%	59%	11%	30%

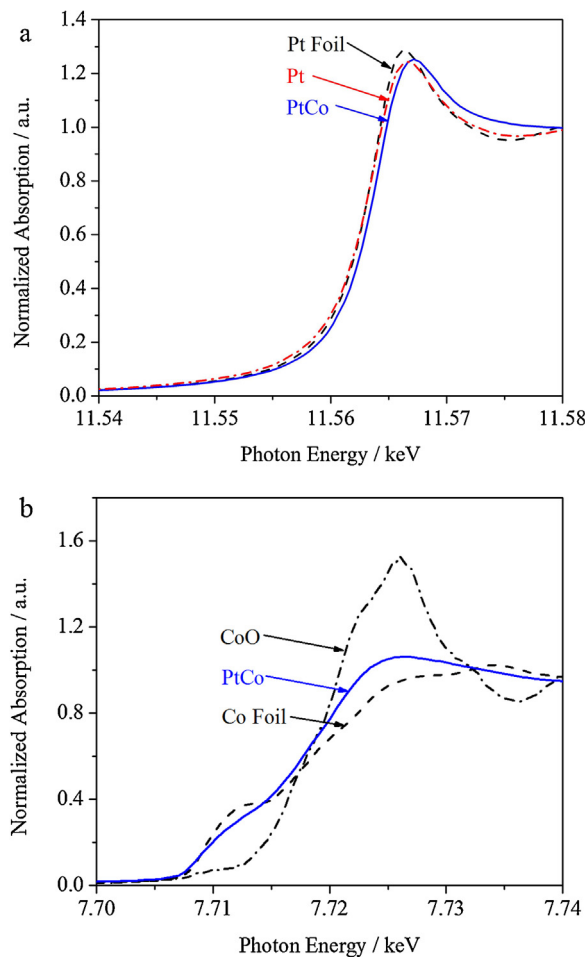


Fig. 5. (a) Pt L_{III} XANES (11.54–11.58 keV) of Pt foil (black, dashed line), fresh monometallic Pt (red, dashed/dotted line) reduced at 400 °C, and fresh PtCo bimetallic catalyst (blue, solid line) reduced at 400 °C, (b) Co K XANES (7.70–7.74 keV) of fresh PtCo catalyst reduced at 400 °C (blue, solid line), Co foil (black, dashed line), and CoO (black, dashed/dotted line). (For interpretation of the references to color in this figure legend, the reader is referred to the web version of this article.)

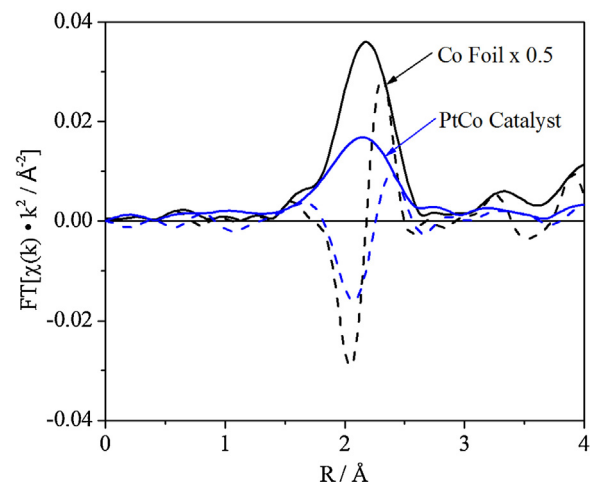


Fig. 7. Magnitude (solid line) and imaginary part (dotted line) of the FT of the Co K edge k^2 -weighted EXAFS for Co foil (black) and fresh PtCo catalyst (blue) reduced at 400 °C. (For interpretation of the references to color in this figure legend, the reader is referred to the web version of this article.)

similar shape to that of the reduced sample indicating that Pt is alloyed with Co. However, a small shift in the edge energy (11.5644 keV for *operando* versus 11.5643 keV for the reduced sample), accompanied by an increase in the intensity of the white line suggests changes to the Pt bonding environment. Performing a similar Δ XANES experiment as described above (Fig. 10), it was observed that there was surface CO under reaction conditions, with a contribution of 60% of that taken under a CO environment at room temperature. These observations are in agreement with our previous characterization of Pt catalysts for APR [18].

The Co K edge XANES for the catalyst under reaction conditions shows an increased degree of oxidation compared to the reduced sample (Fig. 9b). A linear combination using Co foil and CoO as references indicates that the Co remains 70% reduced even under the highly oxidizing water environment. This is in contrast to the monometallic Co sample, which oxidized completely to Co²⁺ when steamed with water at 300 °C (Table S.1). Unlike the Pt edge, where it is possible to perform a Δ XANES experiment to probe the surface

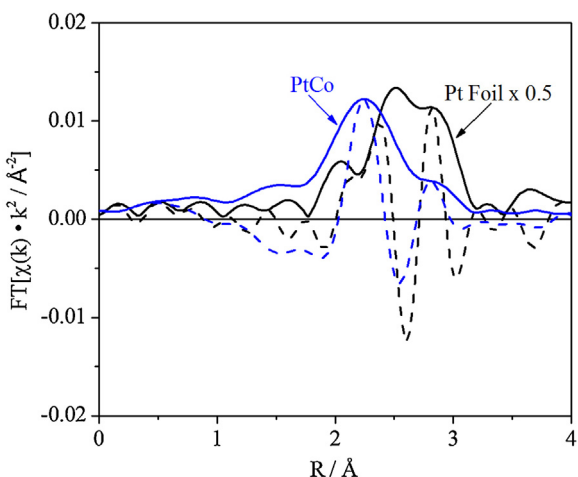


Fig. 6. Magnitude (solid line) and imaginary part (dotted line) of the FT of the Pt L_{III} edge k^2 -weighted EXAFS for a Pt foil (black) and the fresh PtCo catalyst reduced at 400 °C (blue). (For interpretation of the references to color in this figure legend, the reader is referred to the web version of this article.)

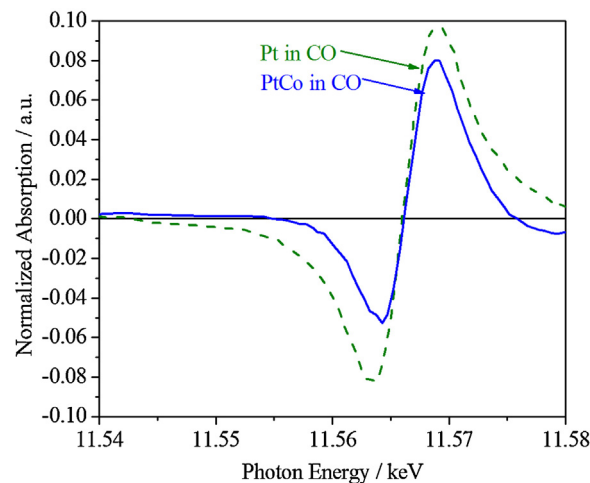


Fig. 8. Pt L_{III} Δ XANES (11.55–11.58 keV) for the fresh PtCo/MWCNT with CO adsorbed (blue, solid line) and a fresh Pt/MWCNT catalyst with CO adsorbed (green, dashed line) (Δ XANES = spectra with adsorbed CO minus that in He). (For interpretation of the references to color in this figure legend, the reader is referred to the web version of this article.)

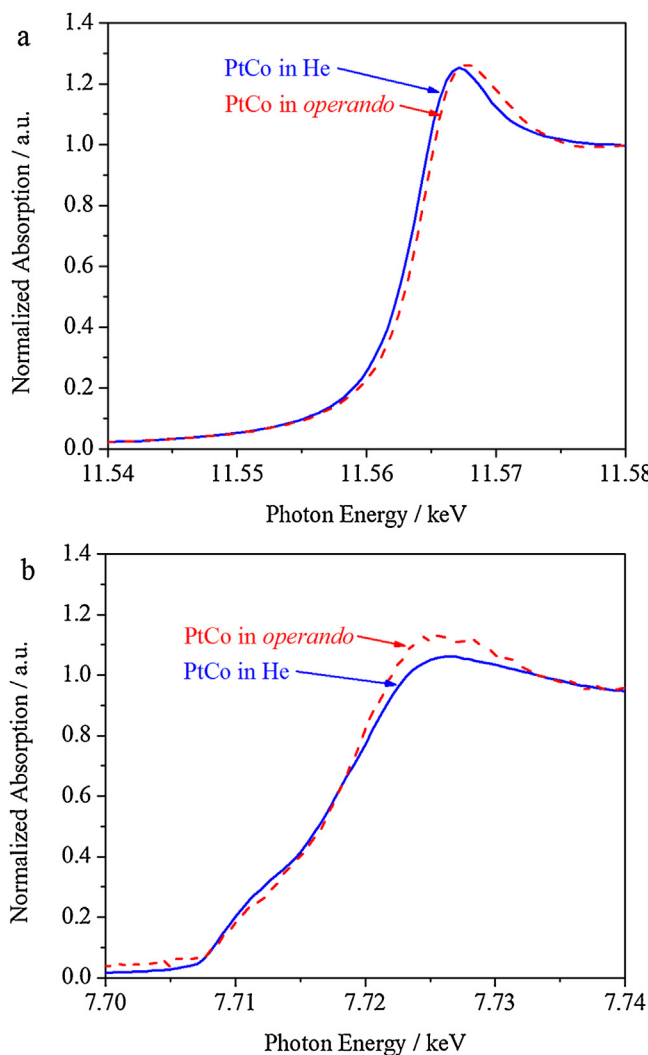


Fig. 9. (a) Pt L_{3,3} edge XANES (11.54–11.58 keV) for the fresh reduced PtCo catalyst (blue, solid line) and the catalyst under *operando* conditions (red, dashed line), (b) Co K edge XANES (7.70–7.74 keV) for the fresh reduced PtCo catalyst (blue) and PtCo catalyst under *operando* conditions (red, dashed line). *Operando* conditions were 230 °C, 32 bar, 30 wt% aqueous glycerol, WHSV = 180 h⁻¹. (For interpretation of the references to color in this figure legend, the reader is referred to the web version of this article.)

species under reaction conditions, the Co K edge is a 1 s to valence transition. This particular electron transition does not probe the bonding states, thus making an analogous Δ XANES experiment impossible to perform.

The Pt and Co *operando* EXAFS results suggest that the bimetallic nature of the particles was maintained under reaction conditions. The FT results for Pt and Co (Fig. S.5) are qualitatively similar to those results obtained for the reduced samples under helium, indicating that there are still bimetallic particles under reaction conditions. However, the fit parameters suggest changes in the configuration of the particles. From the Pt edge, there is an increase in the Pt-Pt coordination (from 4.6 to 7), and a drop in the Pt-Co scattering contribution (2.5–1.8). From the Co edge, it is observed that the Co–Co coordination decreases (3.8–2.1), but the Co–Pt coordination remains nearly the same. The fit Pt–Co and Co–Pt bond distances are not equivalent, however, this is due to Co leaching from the catalyst, the implications of which are discussed in Section 4.2. The bond distances do not change from their corresponding values at room temperature.

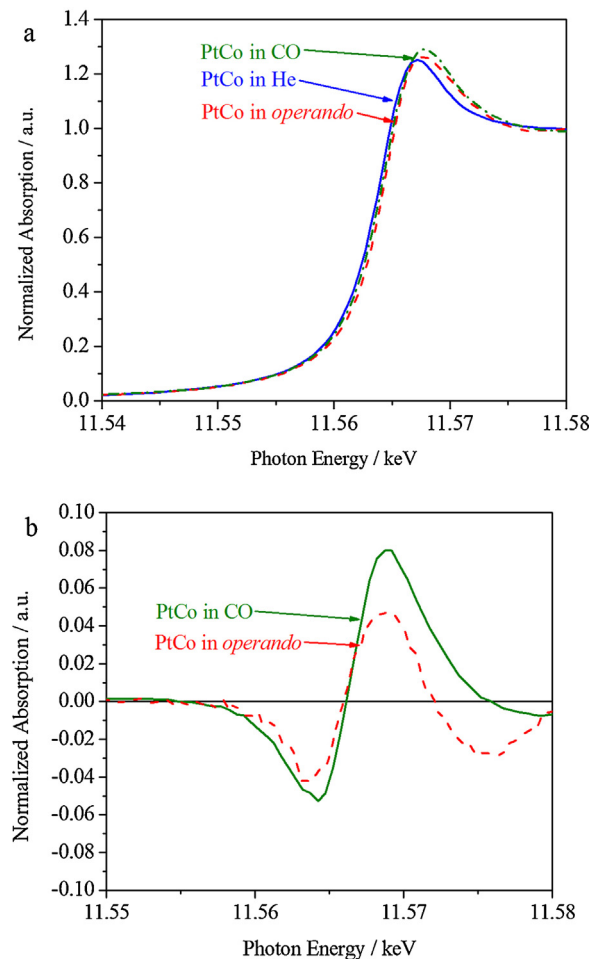


Fig. 10. Pt L_{3,3} XANES result (11.54–11.58 keV) for (a) the PtCo catalyst fresh and reduced in He (blue, solid line), with adsorbed CO (green, dashed/dotted line) and *in operando* under glycerol reforming conditions (red, dashed line), (b) Δ XANES (11.55–11.58 keV) for the PtCo catalyst under *operando* conditions (red, dashed line) and with CO adsorbed under He at RT (green, solid line) (Δ XANES = spectra with adsorbed CO minus that in He). (For interpretation of the references to color in this figure legend, the reader is referred to the web version of this article.)

4. Discussion

4.1. Glycerol reforming pathway

The reaction products identified were consistent with parallel carbon–carbon cleavage ([C–C]) and carbon–oxygen cleavage ([C–O]) pathways. When glycerol undergoes [C–C] cleavage, surface CO (which is observed in the Pt L_{3,3} XANES during *operando* experiments) and H₂ are generated. Under aqueous conditions, the surface CO undergoes the water–gas shift reaction to generate CO₂ and additional H₂. Conversion of molecules with a C:O stoichiometry of 1:1 (i.e., glycerol) completely to CO₂ and H₂ via [C–C] cleavage represents the highest possible hydrogen yields from APR. Conversely, when these molecules undergo [C–O] cleavage, deoxygenated products with unsaturated C=C or C=O fragments are formed. These intermediates are then hydrogenated *in situ* by hydrogen generated through the [C–C] cleavage pathway and form liquid phase intermediates with saturated hydrocarbon fragments. When these intermediates undergo subsequent [C–C] cleavage and convert to gas phase molecules, they consume additional hydrogen and form small alkanes. These reactions represent a significant loss in hydrogen yield. For example, a change in the reaction pathway to produce one mole of CH₄ (i.e. doing a single C–O cleavage) rather

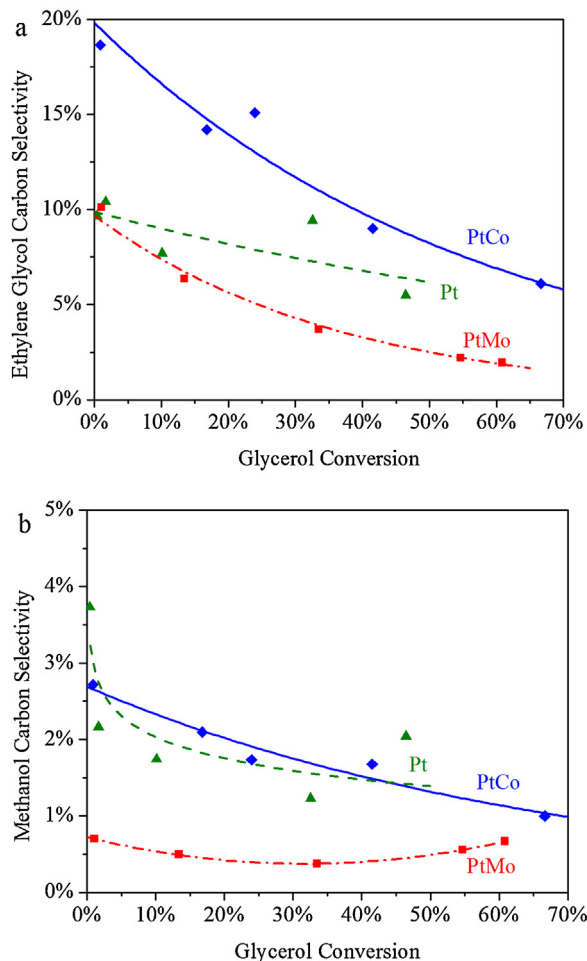


Fig. 11. Selectivity versus glycerol conversion trends for ethylene glycol (a) and methanol (b) for Pt (green, ▲, dashed line), PtMo (red, ■, dashed/dotted line), and PtCo (blue, ♦, solid line). Measurements taken at 230 °C, 32 bar, 30 wt% aqueous glycerol and WHSV between 1 and 200 h⁻¹. (For interpretation of the references to color in this figure legend, the reader is referred to the web version of this article.)

than one mole of CO₂ results in the loss of four moles of H₂ from the final yield. Thus, limiting [C—O] cleavage reactions is essential to maximizing hydrogen yield.

The observed differences in selectivity between Pt, PtCo, and PtMo are the result of differences in the effect of each promoter metal on the pathways and rates of reaction. The carbon selectivity ($(r_{\text{product}} \times \text{Product carbon number})/(r_{\text{glycerol}} \times 3) \times 100\%$) trends for ethylene glycol (EG) and methanol – the liquid phase intermediate products resulting from the carbon–carbon cleavage pathway – and for CO₂ generation, are similar over all three catalysts (Fig. 11), suggesting that the pathway for [C–C] cleavage is similar over all three catalysts. The total selectivity to [C–C] scission products shows the differences in pathway selectivity between the catalysts, however. For example, PtCo has a 5–10% higher selectivity to EG than Pt, but Pt has higher selectivity to CO₂ (0–5% higher at all measured conversions), due to a large increase in EG production STY on PtCo (additional details below). Since both products are the result of only the [C–C] cleavage pathway, if the values are added together (i.e. to give a ‘total’ [C–C] pathway selectivity), they give similar values between 50% and 60% at 1% conversion, which converge to 70% at higher conversions. This is evidence that Pt and PtCo have similar selectivity to the [C–C] pathway. The combined [C–C] selectivity for the PtMo catalyst, however, was around 20% lower at all measured conversions (24% selectivity at 1% conversion, and 50–55% selectivity at higher conversions).

There are also differences in selectivity between Pt, PtCo, and PtMo in the three most abundant [C–O] cleavage products: propylene glycol (PG), ethanol, and 1-propanol (Fig. 12). The Pt and PtCo show similar selectivity values and trends to these products (nearly constant 5% and 2% selectivity to ethanol and 1-propanol, respectively; and a similar profile shape with selectivity between 10% and 20% for PG). However, the PtMo catalyst shows both different selectivity trends and higher selectivity (15–35% higher [C–O] scission selectivity, Fig. 3) to these products, particularly propylene glycol, suggesting that the Mo both increases the site time yields of [C–O] cleavage products and does so by a different mechanism. This is consistent with our previous work, which suggests that the Mo not only modifies the Pt reaction site, but generates additional reaction sites, either as a Mo–O/OH acidic site on the surface of the PtMo particles, or as a Pt–Mo bimetallic pair site, similar to other deoxygenation catalysts in literature [34,35]. The addition of these deoxygenation sites is the reason for the observed differences in selectivity.

The differences in promotional effect between PtMo and PtCo versus Pt catalysts are also apparent in the measured site time yields. At conversion around 1%, the increase in overall reaction STY (glycerol consumption) is of similar magnitude for both PtCo (4.6× STY increase) and PtMo (5.6× STY increase). However, the PtMo catalyst does not show an increase in the hydrogen generation STY, whereas the PtCo has an increase in H₂ STY that is similar to the increase in glycerol conversion rate compared to that for Pt (4.6× increase in glycerol, 3.9× increase in H₂ STY, Table 1). While the apparent site time yield of hydrogen is lower over PtMo (0.6× versus Pt), the site time yields of CO₂ (1.8× versus Pt) and EG (5.5× versus Pt) indicate that the H₂ generation pathway is promoted, but that H₂ is consumed to hydrogenate unsaturated intermediates resulting from [C–O] scission.

The relative promotion of CO₂ and EG ([C–C] pathway), and hydroxyacetone (HA) and propylene glycol ([C–O] pathway) site time yields between the three catalysts also illustrates the differences in the effects of the different promoters. The ratio of CO₂ + EG STY to PG + HA STY are 4.5 for Pt, 6.1 for PtCo and 1.3 for PtMo. The [C–C]/[C–O] STY ratio is higher on PtCo than Pt, but both are at least a factor of 3 higher than on PtMo. The difference in Pt and PtCo STY ratios is accounted for by the fact that PtCo increases the STY of EG by a larger factor than to CO₂ (8.2× for EG, 4.4× for CO₂) versus Pt. This is also why the selectivity to EG is higher on PtCo than it is on Pt, and results in the 5% decrease seen in the CO₂ selectivity, since the total [C–C] selectivity is similar. The EG selectivity on PtMo is lower not because of a lack of a promotional effect (PtMo increases the EG STY by a factor of 5.5 compared to Pt), but rather because the site time yields to HA and PG are promoted by a larger amount (7.5× increase for HA + PG on PtMo versus Pt, compared to 3.5× increase for PtCo versus Pt), resulting in the lower [C–C]/[C–O] STY ratio.

This, in addition to the higher site time yields of deoxygenated intermediates, is the reason why the H₂ site time yield does not appear significantly higher for PtMo versus Pt at low conversion, but an overall promotion still exists. The Mo is increasing the site time yields of both [C–C] and [C–O] cleavage reactions, the former in a similar way as the Co (due to similarities in the pathway intermediates), and the latter by introducing additional deoxygenation sites. By contrast, the PtCo catalyst has similar selectivity profiles for all intermediates and products when compared to the monometallic Pt. The increase in site time yields with very little change in selectivity between Pt and PtCo suggests that the reaction sites are similar between these two catalysts and that the function of Co is to promote Pt functionality.

The consequence of the differences in PtMo and PtCo promotion on the ability of these catalysts to effectively generate H₂ are most evident in the gas phase H₂ selectivity (Fig. 2), particularly at conversion above 50% where many of the liquid phase intermediates

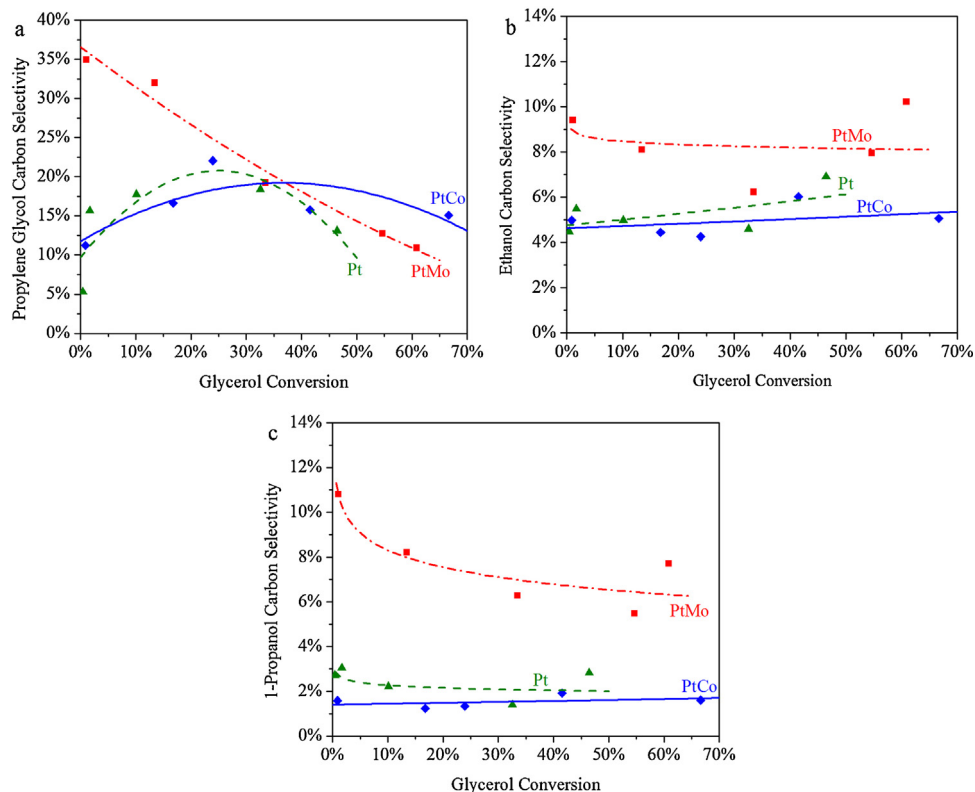


Fig. 12. Selectivity versus glycerol conversion trends for (a) propylene glycol, (b) ethanol, and (c) 1-propanol for Pt (green, ▲, dashed line), PtMo (red, ■, dashed/dotted line), and PtCo (blue, ♦, solid line). Measurements taken at 230 °C, 32 bar, 30 wt% aqueous glycerol, and WHSV between 1 and 200 h⁻¹. (For interpretation of the references to color in this figure legend, the reader is referred to the web version of this article.)

resulting from [C–O] scission are further converted (>60% selectivity to gas phase products), resulting in a large decrease in the PtMo H₂ selectivity from 82% to 65% as more hydrocarbon fragments are produced, versus only a small decrease in the PtCo and Pt selectivity (from 96% to 92% and 90% to 85%).

We also note that both PtMo and PtCo show a promotional effect for the water–gas shift (WGS) reaction compared to the monometallic Pt (Table 1). The observed increase in both APR site time yields and WGS rates suggests that these two reactions are related. The presence of CO on the surface of the catalyst during APR, but low CO levels relative to CO₂ in the gas phase effluent (CO₂:CO ratios > 100:1), suggests that the water–gas shift reaction is an important part of the reforming reaction network. Carbon monoxide binds strongly to Pt surfaces and is a well known poison for Pt catalysts, and in this case the role of WGS may be to assist in removing from the surface CO species that are generated by the [C–C] cleavage pathway and detected by the *operando* ΔXANES experiments. A more in-depth study on the link between APR and WGS is currently under investigation by our group, and will be the subject of a future report.

4.2. The active catalyst structure and effects of reaction environment on structure

The STEM results on the used sample shows that the catalyst does not have a homogenous composition, but rather contains contributions from several different particle types. The fit parameters listed in Table S.1, particularly for the sample *in operando*, are generally consistent with the different particle configurations determined from the STEM-EELS line scans, which suggest that there are discreet Pt–Pt and Co–Co phases (i.e., Pt only particles, core/shell particles with Co- and Pt-rich phases), but also mixed phases (well mixed alloy particles, core/shell Co–Pt interface).

The large average Pt–Pt CN (7) compared to smaller Pt–Co CN is consistent with having a significant fraction of monometallic particles compared to bimetallic particles (~60% of the particles are monometallic Pt by STEM), and generally Pt rich particles. The Co fit parameters were also determined as an average over all the Co atoms in the sample, but 70% of the Co was fully reduced by *operando* XANES. If just the metallic portion is considered, the true coordination numbers will be $N_{\text{fit}}/\text{fraction Co}^0$, or $N_{\text{fit}}/0.7$. This means that the true Co–Co and Co–Pt CNs for only the metallic Co are 3 and 3.9. In a similar manner, if assumptions are made about how the molar fractions of Pt are distributed between monometallic and bimetallic particles, the contribution from the bimetallic particles to the measured Pt–Pt coordination can be estimated. As an example, if the molar fraction of the Pt in bimetallic particles is assumed to be 50%, the true coordination numbers for the Pt–X scatters are 6.9 and 3.6 for Pt–Pt and Pt–Co. These calculated ‘true N’ are consistent with coordination numbers that might be expected for the particle configurations as determined by STEM for both Pt shell/Co core particles, and Pt rich alloy particles. Similar calculations were made for several different distributions of Pt assuming that the Pt only particles were 2.2 nm (from the TEM), and can be found in the supplementary information along with the method for calculating these values (Table S.3). The total coordination numbers for the Pt edge were compared to the total coordination number expected for particles of 3–4 nm (the bimetallic particles in the STEM appeared to be larger than the monometallic particles) based on the correlation of Miller et al. [30] to determine the feasibility of the assumed metal distribution. By this method, the bimetallic particles were estimated to contain between 50% and 80% of the Pt. In general, the total Pt coordination (>9) was higher than the total Co coordination (6.9) for the contributions from the bimetallic particles, with high Pt–Pt CN (6.8–6.9), suggesting overall Pt-rich bimetallic particles.

The stability of the PtCo bimetallic structures under reaction conditions are also of interest. Evidence for Co leaching was observed in the analysis of the liquid phase effluent from APR over PtCo catalysts by atomic absorption spectroscopy shows the presence of Co in solution (used to detect but not quantify), which was not present in the reaction effluent of either Pt or PtMo catalysts (indicating that it is not a false positive caused by organic reaction products, for example). Additional evidence was observed in the differences in edge step for the Co XANES of PtCo catalyst in the *operando* reactor before introduction of the feed and during reaction. Under these cases, the edge step dropped from 0.83 (fresh) to 0.36 (*in operando*). Since the edge step is linearly related to the number of absorbers, and the same position in the bed was used for both measurements, the drop in edge step is related to the loss of Co from the sample. The fraction of remaining Co can be estimated from the ratio of the edge step, that is 0.36/0.83, or about 40% of the initial Co remains.

In addition, the loss of Co can be used to explain why the Co-Pt and Pt-Co no longer match as they do in the reduced sample. However, we can use the estimated Co loss from the XANES to correct the equation $CN_{Pt-Co} \cdot (\text{atoms Pt}) = CN_{Co-Pt} \cdot (\text{atoms Co})$ [29]. In the fresh sample, $(\text{atoms a}) = (\text{atoms b})$, however, after accounting for Co leaching, $(\text{atoms Co})_{\text{operando}} = 0.43 \cdot (\text{atoms Co})_{\text{initial}}$. Since Pt does not leach and $(\text{atoms Co})_{\text{initial}} = (\text{atoms Pt})$, the above equation becomes $CN_{Pt-Co} = CN_{Co-Pt} \cdot 0.43$. If the experimental CNs are plugged in, we have $CN_{Pt-Co} = 1.8$ and $CN_{Co-Pt} = 1.2$. These coordination numbers are generally consistent in light of the uncertainty in the estimate of the fraction of Co loss using XANES, as well as the errors inherent in the calculated fitting parameters.

These losses are consistent with results from electrochemistry, which described Co leaching from CoO species and non-ordered PtCo alloys under acidic conditions leaving Pt-rich species [36–38]. Additionally, it was noted that lower temperature pretreatment led to a higher degree of leaching due to incomplete alloying of Pt and Co [36]. In light of the STEM results, which showed several different particle configurations, as well as the sequential IWI synthesis method and low pretreatment temperature (400 °C), it is likely that the fresh catalyst contains Co only particles as well as multiple types of PtCo bimetallic or alloy particles. The presence of Pt shell/Co core particles is consistent with leaching Co from unstable alloy particles, as leaching has been demonstrated to leave Pt-skin type particles similar to the core/shell particles observed in the STEM [38]. However, the STEM results show the presence of a stable PtCo alloy phase after the reaction. One possibility for this alloy phase is ordered PtCo alloys, which were stable after harsh conditions such as acid treatments at a pH of 1 and electrochemical reaction cycles [37]. However, these treatments were performed at room temperature, and so these ordered structures may not be stable at the elevated temperatures and pressures in the APR reactors.

Most importantly, despite the loss of Co, the catalyst was stable for over one week on stream (Fig. S.6). It is possible that the catalyst deactivates significantly over the first few hours as the initial leaching from unstable Co species occurs. However, any Co in liquid samples collected near the end of the run was below the detection limit of 9 ppm and the remaining bimetallic structures did not change after reaction (the EXAFS fits for catalysts after one week of reaction matched those taken under *operando* conditions after 12–18 h of operation), which indicates that the particle rearrangement and leaching happens during the initial line-out period, and that the particle type distributions observed on the spent samples are similar to the particle type distributions in the working catalyst. Coupled with the stability data, this means that the remaining PtCo bimetallic particles which contribute to the steady-state promotion are stable.

4.3. Effect of catalyst structure on catalytic activity

The activity and selectivity trends were related to the observed catalyst structure from the characterization. Both STEM and XAS indicate that the bimetallic PtCo particles take on configurations that contain significant surface Pt, and the ΔXANES analysis for CO adsorption on the PtCo catalyst indicates that about 65% of the particle surface is Pt. These results suggest that the particles have generally Pt-rich surfaces. The PtMo catalyst adopts a different configuration, with a Pt rich core and a Mo rich PtMo surface layer [17], with an estimated surface Pt fraction of only about 25% by ΔXANES. The ΔXANES results are qualitatively similar to CO chemisorption results, which indicate a 48% dispersion for Pt, 35% dispersion for PtCo (72% Pt surface fraction compared to Pt), and 20% dispersion for PtMo (42% surface fraction). The differences in Pt surface fractions determined by ΔXANES and chemisorption may be due to CO adsorption on the secondary metals on the surface, since the surface fractions calculated from ΔXANES were lower than the chemisorption surface fractions. However, the small differences between the results suggest that predominant sites for CO adsorption on these catalysts are surface Pt sites (as the ΔXANES is Pt specific).

These differences in available surface Pt have an effect on the selectivity differences observed over the catalysts. Density functional theory calculations [39,40] indicate that Pt surfaces are selective to [C–C] cleavage reactions, suggesting that catalysts with high surface Pt content are selective toward hydrogen generation. The predominantly Pt-rich surfaces on PtCo catalysts are the appropriate reaction sites for [C–C] cleavage reactions and help maintain the Pt-like selectivity. For the PtMo case, the presence of Mo on the surface both limits the availability of Pt for the [C–C] cleavage reactions and introduces bimetallic Pt–Mo or Pt–MoO_x/OH acid sites that have been demonstrated in the literature to catalyze [C–O] cleavage reactions [18,34,35].

Despite changing the reaction selectivity, the Co and Mo have similar effects on the rate of reaction. We have noted above the importance of the water–gas shift reaction in the reforming network as a method by which CO species generated during reforming are removed from the catalyst surface. One way that the secondary metal may promote the APR reaction is by facilitating the water–gas shift reaction on surface CO species to turn over the Pt-based reaction sites. Previous results suggest that the role of exposed Mo or MoO_x is to increase the rate of water dissociation in the water–gas shift reaction by providing water activation sites [26]. Thus, the rate promoting effect may be due to the presence of a Mo species on the surface of the PtMo bimetallic particles, which promotes the rate of the surface-cleaning WGS reaction by increasing the availability of surface hydroxyls near the Pt sites. Similarly, surface Co species on the well-mixed alloy particles (as alloyed metallic Co or stable surface CoO) may act as water activation sites to increase the coverage of surface hydroxyls, similar to the role of Mo proposed above, thereby increasing surface water–gas shift rates to remove the CO and turn over the reaction sites. The CO ΔXANES experiments showed that 65% of the surface was Pt, with cobalt making up the remaining 35%. As noted above, the presence of cobalt-only particles were not found in the STEM images, nor was there any evidence of Co or CoO surrounding the particles, indicating the only Co on the sample was that which was coordinated with Pt.

An additional mechanism by which the alloying may help the rate of reaction is by modification of the CO binding energy. The changes to the XANES (increase in white line intensity relative to monometallic Pt and a broadening of the white line) are consistent with downward shifts in the d-band center [41]. This downward shift in the d-band shift has been demonstrated in the literature to correspond to generally lower binding energies of surface species such as CO [42–45]. Since the CO is generated on the surface by reactions of the parent oxygenate molecules, a lower binding

energy may assist in promoting the reaction by removing surface CO species by desorption, in addition to removal of the CO via WGS.

Finally, we note that the STEM-EELS line scans show a significant fraction of monometallic Pt particles for the PtCo samples. Despite this, there is still a measurable increase in the reaction rates as the result of adding Co to Pt. This promotion is not caused by isolated Co particles, as the monometallic Co catalyst was ineffective for APR and no Co-only particles were observed in the STEM images. Thus, the promotional effect of the Co is the result of forming bimetallic PtCo particles, which are a small fraction of the counted particles (40%). This result also suggests that increasing the fraction of PtCo bimetallic particles on the catalyst should lead to additional rate promotion. However, due to the inhomogeneous distribution of particle types on the PtCo catalyst, it is difficult to distinguish which PtCo phase(s) are responsible for the promotional effect and to fully quantify their effects. A more in depth study on the PtCo system for aqueous phase reforming has been performed by our group to study the relationship between particle type distribution and catalyst site time yield, and is a more quantitative analysis of the promotional effect of each particle type [46].

5. Conclusions

The addition of Co and Mo to a Pt aqueous phase reforming catalyst resulted in promotion in overall site time yields (five- and sixfold increase at 1% conversion), but different effects on the hydrogen generation site time yields (fourfold H₂ STY increase for PtCo versus Pt and no H₂ STY increase for PtMo versus Pt, at 1% conversion). The observed STY differences are the result of different selectivity for PtMo versus PtCo, with PtMo promoting deoxygenation reactions which form undesired alkane side products and reduce the H₂ yield in higher proportion relative to the STYs of the hydrogen generation pathway than does PtCo. At glycerol conversions above 60%, this manifests itself as a 20% difference in gas phase H₂ selectivity (85% for PtCo, and 65% for PtMo).

The observed differences in the site time yields and selectivity observed over PtCo and PtMo catalysts are the results of the active structures of the catalyst. Both secondary metals provide improvements in the rate of the hydrogen generation pathway by adding water activation sites that improve the rate of surface water–gas shift to remove surface CO (observed in the *operando* ΔXANES) generated in the reforming pathway. However, in addition to providing water activation, the surface Mo species can act as deoxygenation sites (as either PtMo bimetallic pairs or Pt–MoO₄/OH acid sites), which cause the observed changes to selectivity.

The changes to the EXAFS for the PtCo catalyst and Co detected in the liquid phase effluent are evidence of leaching of the secondary metal. This leaching results in the predominantly Pt-rich particles observed in the STEM, but the presence of well-mixed PtCo alloy particles after reaction indicate that there is a form of PtCo alloy that is stable under APR conditions. The small number of bimetallic particles coupled with the observed site time yield improvements suggest that the performance could be improved with synthesis methods that selectively create the stable forms of the bimetallic particles.

Acknowledgments

This material is based upon work supported as part of the Institute for Atom-efficient Chemical Transformations (IACT), an Energy Frontier Research Center funded by the U.S. Department of Energy, Office of Science, Office of Basic Energy Sciences. Use of the Advanced Photon Source is supported by the U.S. Department of Energy, Office of Science, and Office of Basic Energy Sciences, under Contract DE-AC02-06CH11357. MRCAT operations are supported

by the Department of Energy and the MRCAT member institutions. Scanning transmission electron microscopy was carried out at the Center for Functional Nanomaterials, Brookhaven National Laboratory, which is supported by the U.S. Department of Energy, Office of Basic Energy Sciences, under Contract No. DE-AC02-98CH10886. The authors would like to thank Kaiwalya Sabnis and Yanran Cui for their assistance in collecting the water–gas shift reaction data.

Appendix A. Supplementary data

Supplementary material related to this article can be found, in the online version, at <http://dx.doi.org/10.1016/j.apcatb.2014.03.016>.

References

- [1] A.V. Bridgwater, G.V.C. Peacocke, Renew. Sustain. Energy Rev. 4 (2000) 1–73.
- [2] J.N. Chheda, G.W. Huber, J.A. Dumesic, Angew. Chem. Int. Ed. 46 (2007) 7164–7183.
- [3] D.M. Alonso, J.Q. Bond, J.A. Dumesic, Green Chem. 12 (2010) 1493–1513.
- [4] R.D. Cortright, R.R. Davda, J.A. Dumesic, Nature 418 (2002) 964–967.
- [5] R.R. Davda, J.W. Shabaker, G.W. Huber, R.D. Cortright, J.A. Dumesic, Appl. Catal. B: Environ. 56 (2005) 171–186.
- [6] N. Luo, F. Cao, X. Zhao, T. Xiao, D. Fang, Fuel 86 (2007) 1727–1736.
- [7] J.W. Shabaker, G.W. Huber, R.R. Davda, R.D. Cortright, J.A. Dumesic, Catal. Lett. 88 (2003) 1–8.
- [8] J.W. Shabaker, R.R. Davda, G.W. Huber, R.D. Cortright, J.A. Dumesic, J. Catal. 215 (2003) 344–352.
- [9] R.R. Davda, J.W. Shabaker, G.W. Huber, R.D. Cortright, J.A. Dumesic, Appl. Catal. B: Environ. 43 (2003) 13–26.
- [10] G.W. Huber, J.W. Shabaker, S.T. Evans, J.A. Dumesic, Appl. Catal. B: Environ. 62 (2006) 226–235.
- [11] A. Iriondo, J.F. Cambra, V.L. Barrio, M.B. Guemez, P.L. Arias, M.C. Sanchez-Sanchez, R.M. Navarro, J.L.G. Fierro, Appl. Catal. B: Environ. 106 (2011) 83–93.
- [12] E.L. Kunkes, D.A. Simonetti, J.A. Dumesic, W.D. Pyrz, L.E. Murillo, J.G. Chen, D.J. Buttrey, J. Catal. 260 (2008) 164–177.
- [13] D.L. King, L. Zhang, G. Xia, A.M. Karim, D.J. Heldebrant, X. Wang, T. Peterson, Y. Wang, Appl. Catal. B: Environ. 99 (2010) 206–213.
- [14] E.L. Kunkes, D.A. Simonetti, R.M. West, J.C. Serrano-Ruiz, C.A. Gärtner, J.A. Dumesic, Science 322 (2008) 417–421.
- [15] R.M. West, E.L. Kunkes, D.A. Simonetti, J.A. Dumesic, Catal. Today 147 (2009) 115–125.
- [16] R.R. Soares, D.A. Simonetti, J.A. Dumesic, Angew. Chem. Int. Ed. 45 (2006) 3982–3985.
- [17] P. Dietrich, R. Lobo-Lapidus, T. Wu, A. Sumer, M. Akata, B. Fingland, N. Guo, J. Dumesic, C. Marshall, E. Stach, J. Jellinek, W. Delgass, F. Ribeiro, J. Miller, Top. Catal. 55 (2012) 53–69.
- [18] P.J. Dietrich, T. Wu, M.C. Akata, J.A. Dumesic, J. Jellinek, W.N. Delgass, F.H. Ribeiro, J.T. Miller, Top. Catal. 56 (2013) 1814–1828.
- [19] O. Skoplyak, C. Menning, M. Bartea, J. Chen, Top. Catal. 51 (2008) 49–59.
- [20] O. Skoplyak, M.A. Bartea, J.G. Chen, Catal. Today 147 (2009) 150–157.
- [21] X. Wang, N. Li, L.D. Pfefferle, G.L. Haller, Catal. Today 146 (2009) 160–165.
- [22] X. Wang, N. Li, L.D. Pfefferle, G.L. Haller, J. Phys. Chem. C 114 (2010) 16996–17002.
- [23] P. Serp, M. Corrias, P. Kalck, Appl. Catal. A: Gen. 253 (2003) 337–358.
- [24] B. Fingland, F. Ribeiro, J. Miller, Catal. Lett. 131 (2009) 1–6.
- [25] V.F. Kispersky, A.J. Kropf, F.H. Ribeiro, J.T. Miller, Phys. Chem. Chem. Phys. 14 (2012) 2229–2238.
- [26] W.D. Williams, L. Bollmann, J.T. Miller, W.N. Delgass, F.H. Ribeiro, Appl. Catal. B: Environ. 125 (2012) 206–214.
- [27] Y. Lei, J. Jelic, L. Nitsche, R. Meyer, J. Miller, Top. Catal. 54 (2011) 334–348.
- [28] J.A. van Bokhoven, J.T. Miller, J. Phys. Chem. C 111 (2007) 9245–9249.
- [29] G.H. Via, K.F. Drake Jr., G. Meitzner, F.W. Lytle, J.H. Sinfelt, Catal. Lett. 5 (1990) 25–33.
- [30] J.T. Miller, A.J. Kropf, Y. Zha, J.R. Regalbuto, L. Delannoy, C. Louis, E. Bus, J.A. van Bokhoven, J. Catal. 240 (2006) 222–234.
- [31] N. Guo, B.R. Fingland, W.D. Williams, V.F. Kispersky, J. Jelic, W.N. Delgass, F.H. Ribeiro, R.J. Meyer, J.T. Miller, Phys. Chem. Chem. Phys. 12 (2010) 5678–5693.
- [32] A.Y. Stakheev, Y. Zhang, A.V. Ivanov, G.N. Baeva, D.E. Ramaker, D.C. Koningsberger, J. Phys. Chem. C 111 (2007) 3938–3948.
- [33] D. Shriner, P. Atkins, T. Overton, J. Rourke, Inorganic Chemistry, Oxford University Press, Oxford, UK, 2009.
- [34] M. Chia, Y.J. Pagán-Torres, D. Hibbitts, Q. Tan, H.N. Pham, A.K. Datye, M. Neurock, R.J. Davis, J.A. Dumesic, J. Am. Chem. Soc. 133 (2011) 12675–12689.
- [35] S. Koso, N. Ueda, Y. Shinmi, K. Okumura, T. Kizuka, K. Tomishige, J. Catal. 267 (2009) 89–92.
- [36] E. Antolini, J.R.C. Salgado, E.R. Gonzalez, J. Power Sources 160 (2006) 957–968.
- [37] S. Koh, J. Leisch, M.F. Toney, P. Strasser, J. Phys. Chem. C 111 (2007) 3744–3752.
- [38] V.R. Stamenkovic, B.S. Mun, K.J.J. Mayrhofer, P.N. Ross, N.M. Markovic, J. Am. Chem. Soc. 128 (2006) 8813–8819.
- [39] B. Liu, J. Greeley, Top. Catal. 55 (2012) 280–289.

- [40] B. Liu, J. Greeley, *J. Phys. Chem. C* 115 (2011) 19702–19709.
- [41] N. Schweitzer, H. Xin, E. Nikolla, J. Miller, S. Linic, *Top. Catal.* 53 (2010) 348–356.
- [42] J.R. Kitchin, J.K. Nørskov, M.A. Bartheau, J.G. Chen, *J. Chem. Phys.* (2004) 10240–10246.
- [43] M. Mavrikakis, B. Hammer, J.K. Nørskov, *Phys. Rev. Lett.* 81 (1998) 2819–2822.
- [44] A. Ruban, B. Hammer, P. Stoltze, H.L. Skriver, J.K. Nørskov, *J. Mol. Catal. A: Chem.* 115 (1997) 421–429.
- [45] B. Hammer, J.K. Nørskov, in: H.K. Bruce, C. Gates (Eds.), *Advances in Catalysis*, Academic Press, Amsterdam, The Netherlands, 2000, pp. 71–129.
- [46] P.J. Dietrich, M.C. Akatay, F.G. Sollberger, E.A. Stach, J.T. Miller, W.N. Delgass, F.H. Ribeiro, *ACS Catal.* 4 (2014) 480–491.